

First Principles Determination of the Potential-of-zero-charge in an Alumina-coated Aluminum/Water Interface Model for Corrosion Applications

Kevin Leung*

*Sandia National Laboratories, MS 1415,
Albuquerque, NM 87185*

*kleung@sandia.gov

(Dated: October 13, 2022)

Abstract

The surfaces of most metals immersed in aqueous electrolytes have a several-nanometer-thick oxide/hydroxide surface layer. This gives rise to the existence of both metal|oxide and oxide|liquid electrolyte interfaces, and makes it challenging to correlate atomic length-scale structures with electrochemical properties such the potential-of-zero-charge (PZC). The PZC has been shown to be correlated the pitting onset potential for corrosion. In this work, we conduct large-scale Density Functional Theory and *ab initio* molecular dynamics to calculate the PZC of a Al(111)| γ -Al₂O₃(110)|water double-interface model within the context of aluminum corrosion. By partitioning the multiple interfaces involved into binary components with additive contributions to the overall work function and voltage, we predict the PZC to be -1.53 V vs. SHE for this model. We also calculate the orbital energy levels of defects like oxygen vacancies in the oxide, which are critical parameters in theories associated with pitting corrosion. We predict that the Fermi level at the PZC lies above the impurity defect levels of the oxygen vacancies, which are therefore uncharged at the PZC. From the PZC estimate, we predict the voltage needed to create oxygen vacancies with net positive charges within a flat-band approximation.

I. INTRODUCTION

Corrosion¹ involves complex interfaces and processes that have so far defied quantitative elucidation using atomic length-scale calculations. One challenging aspect is the surface-film-covered (non-pristine) nature of metal/liquid electrolyte interfaces. Net charges can exist at the oxide/electrolyte interface via acid-base reactions at surface hydroxyl (-OH) sites, compensated by the electric double layer (EDL) in the liquid electrolyte immediately outside the passivating oxide film.²⁻⁴ Charges can also exist in defect sites in the oxide film itself, or at the metal|oxide interface (Fig. 1a).^{5,6} This complexity makes electrochemical properties like the potential-of-zero-charge (PZC) far more difficult to predict using atomic length-scale methods than those for pristine electrodes without surface films.⁷⁻¹⁰

The PZC is of significant interest because PZC's of a set of metal alloys have been demonstrated to be linearly correlated to the pitting (onset) potentials.^{3,11} It is also correlated to the pH-of-zero-charge ("pH_{PZC}", or sometime the "isoelectric point").²⁻⁴ In turn, pH_{PZC}'s have been correlated with the pH's-of-zero-charge in pure oxides.² From an atomic length-scale computational viewpoint, the PZC is an equilibrium property which should be amenable to modeling studies. At the PZC, metal|oxide|electrolyte systems exhibit no overall electric field, and are at the "flat band" condition¹² which should be the most straight-forward to model. In contrast, the pitting potential,^{11,13} while critical to understanding corrosion, is a kinetic property, involves extensive chemical reactions, and its prediction is far beyond the current capability of atomic modeling methods.

In particular, Density Functional Theory (DFT) predictions of PZC's will help establish voltage-function relationships which have been largely lacking in current DFT modeling of explicit metal|oxide interfaces.^{6,14-19} For example, Ref. 6 predicted that uncharged oxygen vacancies (V_O^0) give way to charged V_O^{2+} upon applying a sufficient electric field via adding a negative charge at the outer oxide surface. This is significant because V_O^{2+} , and not V_O^0 , are foundational assumptions of the point defect model (PDM) for corrosion,^{5,20-23} which is one of several theories associated with passivation film breakdown.^{14,24-30} However, the voltage associated with this electric field was not elucidated in Ref. 6, partly because it was sensitive to the surface water configuration computed using a sub-monolayer of water frozen at T=0 K. Therefore the predictions could not be directly compared with measurements performed at particular voltages.⁶

Here we adopt a bulk-like liquid water boundary condition, using *ab initio* molecular dynamics (AIMD) to treat the aqueous environment (Fig. 1a), not monolayers of water at $T=0$ K.⁶ By construction, all surfaces/interfaces are uncharged. Thus our models correspond to the PZC, flat band condition; the electrolyte is pure water and automatically accounts for the pH-of-zero-charge condition. We will compute the voltage vs. the Standard Hydrogen Electrode (SHE) reference using the work function approach.^{6,31,32} Since it is costly to apply AIMD to the entire model (Fig. 1a), we split the interfacial contributions to the voltage/work function into four parts (Fig. 1b-e), and add up the components. Such a decomposition would have been more challenging if surface charges and electric fields exist in the oxide film.

Experimentally, Al with anodized oxide films have been estimated to exhibit a PZC at about -1 V vs. SHE (Fig. 1f).¹¹ A flat band potential of ~ 0.7 V has also been reported;³ the discrepancy may be due to the oxide film structure and/or experimental conditions. The true oxide films associated with these experiments are too complex for DFT modeling.¹¹ They have varying Al:O atomic ratios which suggest a finite oxyhydroxide (e.g., AlOOH) content, and exhibit negative space charges, which have been explained in DFT modeling of amorphous oxides.^{34,35} Instead, we focus on the γ -phase Al_2O_3 which has a lower density and should be a better description of amorphous Al_2O_3 ³⁴⁻³⁶ than the α -phase.⁶ We compare the DFT-computed PZC with experimental values, and rationalize the difference in terms of the model oxide structure. As the precise atomic length-scale structures of passivating oxide films and their interfaces are not known experimentally, we argue that, in the future, we should construct models that reproduce the experimental PZC. In other words, calculated voltages should be treated as constraints for model construction, and not as “predictions.”

Finally, we calculate the alignment between a V_{O}^0 in the oxide film and the Al metal Fermi level (E_{F}) pegged to the PZC. This alignment allows us to estimate the voltage, offset from the PZC, at which this particular model exhibits a net charge (i.e., becomes V_{O}^{2+}) within a flat band approximation, and compare it with the experimental pitting potential. We hypothesize that the voltage-induced onset of positively charged oxygen vacancies is hypothesized to be key to corrosion. As will be shown, and has been shown for the α - Al_2O_3 model, the oxygen vacancy orbital levels are filled at PZC conditions. Hence it is the vacancies with the highest-lying orbital levels that will be most relevant to this study. We find that the lowest onset potential of pitting¹³ occurs at potentials sufficiently high that V_{O}^{2+} can exist in the outer region of the oxide film, near the electrolyte. This partially

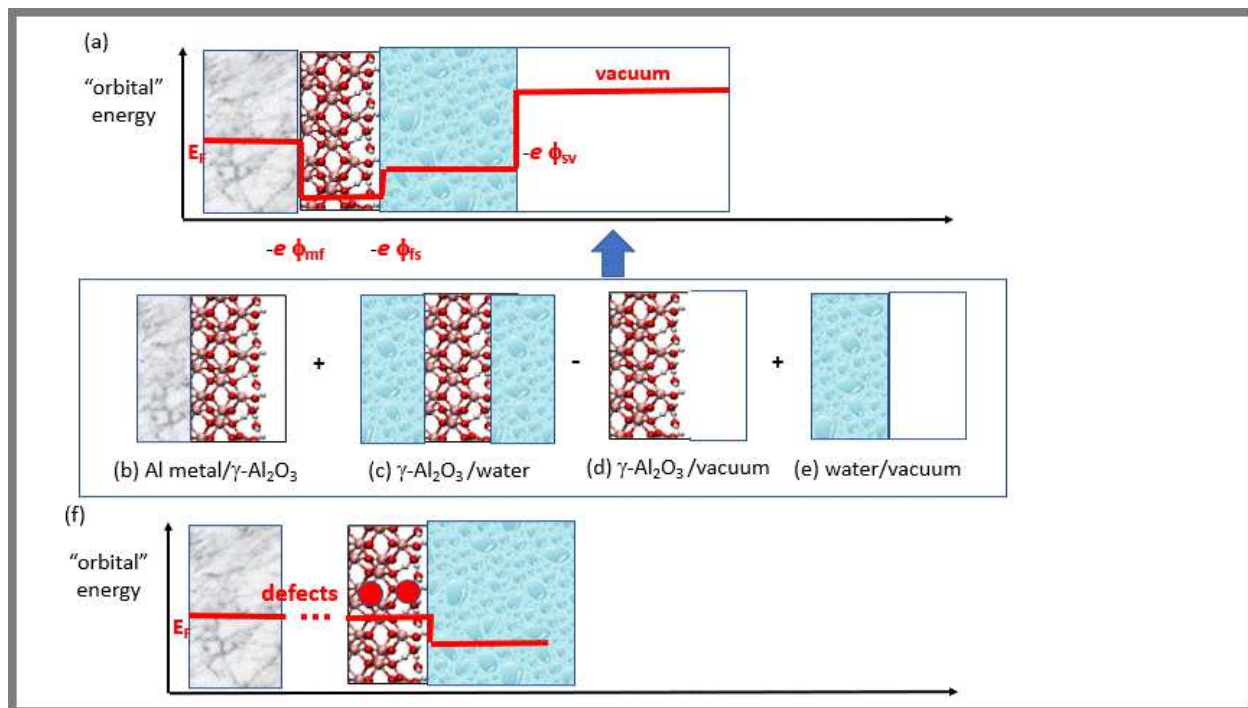


FIG. 1: (a) Schematic of absolute work function for a charge neutral Al| γ -Al₂O₃|water. The work function is related to the voltage; it can be split into four additive contributions: (b) Al| γ -Al₂O₃|vacuum; (c) γ -Al₂O₃|water; (d) the negative of γ -Al₂O₃|vacuum; and (e) water|vacuum. (f) In the experimental literature,¹¹ the metal is often omitted in the analysis. Instead, the Fermi level is assumed to be pinned at defect levels in the oxide, like they would be in semiconductors.

supports the assumptions in the PDM that VO²⁺ exists at the onset of pitting.

This work continues in the vein of our previous work on explicit metal|passivating-layer interfaces for corrosion studies and for batteries.^{6,32,33} The thickness of surface film is explicitly treated as finite, and can be varied from the natural passivating film thickness (no corrosion) to zero (inside corrosion pit), as well as the intermediate, partially decomposed oxide thickness/regime, which may be particularly interesting for corrosion studies. While the present work does not involve cross-film electric fields and cross-film electron transfer reaction,^{32,33} the explicit metal|film models are designed to permit future investigations in that direction.

II. METHOD AND MODELS

A. DFT Details

Most DFT calculations in this work are conducted under ultra-high vacuum (UHV) condition at $T=0$ K, using periodically replicated simulation cells and the Vienna Atomic Simulation Package (VASP) version 5.4.^{38–41} A 400 eV planewave energy cutoff and a 10^{-4} eV energy convergence criterion are enforced. For simulation cells associated with Fig. 1c, *ab initio* molecular dynamics (AIMD) simulations are conducted, using the same energy cutoff, a 10^{-6} eV energy convergence criterion, and a 0.5 fs time-step. The temperature is thermostat at $T=400$ K. Most calculations apply the PBE functional.⁴² In some cases, HSE06 is used for spot checks.^{43–45} Screened long-range exchange DFT functionals have been shown to work reasonably well for metals.⁴⁶ The slightly elevated temperature is needed because the PBE functional yields overstructured water at $T=300$ K.⁴⁷ Some dispersion force corrections can also be used to correct for overstructuring, but those are not applied here. Spin-polarization is turned off because a net spin is found to only accumulate in the metallic region, and it barely affects the total energy.

The metal|oxide and oxide slab models are described in Table I. They contain vacuum regions in the z direction, except the Fig. 1c configuration where the oxide slab is immersed in liquid water on both sides, and a bulk oxide supercell. When a Al(111) metal slab is present at the bottom of the cell, the bottom-most layer of metal atoms is kept frozen. The bulk and (110) surface structures of γ -Al₂O₃ are taken from Ref. 48, except that we enforce an orthonormal unit cell and set to zero the small deviation of the γ angle from 90°. The change in energy with this constraint is less than 0.02 eV per γ -Al₂O₃ unit cell containing 40 atoms. Apart from the lowest energy (110) surface cut from Ref. 48 (henceforth referred to as the “A-cut,”) we also consider a slightly higher surface energy cut of this surface (“B-cut,,” Fig. 2).

We prepare the Al(111)| γ -Al₂O₃(110) interface by placing the metal and the oxide slabs together, and then conducting AIMD simulations at $T=500$ K for 28.2 ps using a 2 fs time step. The oxide lattice constants are used, resulting in expanding the Al lattice constants by 1%. The oxide is approximately 18 Å thick, assuming all atoms have 3.0 Å radii. As will be discussed in Fig. 2 below, this thickness is adequate to yield a bulk-like band-

gap region; however, an even thicker oxide will be ideal in future studies. The final AIMD configuration is quenched from 500 K to 50 K over 3.6 ps, and then optimized. This annealing procedure lowers the total energy of the 510-atom cell (Table I) by 1.50 eV. In the literature, a grid search approach, displacing the two slabs laterally by a small increment followed by a configuration optimization, and repeating using a different increment, has often been applied. Thus we also attempt a restricted grid search by displacing the initial oxide and metal later registry in 1 Å increments in a 8×8 grid. Strictly speaking, the size of the interface cell (Table 1) should require a 8×24 grid, but the total energies are found to be so high, and variations in work functions are so minor, that an expanded search is deemed unlikely to produce an interfacial structure more favorable than the AIMD-annealed one, or one that will yield a very different work function. In this work, we focus on a single, AIMD-equilibrated Al| γ -Al₂O₃ interface. Unlike our previous work,⁶ no model with both metal|oxide and oxide|surface-hydroxide interfaces is used, and the physics associated with the variation this interfacial structure with properties like the oxide/water interface is not considered. A more systematic study will be conducted in the future.

Configurations associated with Fig. 1c are initiated by freezing the γ -Al₂O₃ (110) slab at its DFT optimized configuration, with a partially dissociated monolayer water from Ref. 48 on top and bottom, and applying grand canonical Monte Carlo (GCMC)⁴⁹ with a classical force fields⁵⁰ to populate the vacuum region with liquid water. From the final GCMC configuration, we initiate AIMD simulations at the slightly elevated temperature of T=400 K. During AIMD trajectories, H⁺ transfer between H₂O and AlOH groups at oxide/water interfaces can take place via the Grotthuss mechanism.

Our simulations of oxide-coated Al metal in contact with liquid water are relevant to both pitting corrosion of structural Al metal immersed in aqueous media and to atmospheric corrosion, e.g., for microelectronics applications.⁵¹ At atmospheric conditions, the number of water layers residing on the outer surface of the oxide film depends on the humidity but usually exceed a few nanometer in thickness.^{52,53} We focus on charge-neutral interfaces with no electric double layers in the electrolyte, and assume that ~12-18 Å thick pure water films suffice. A system size convergence check is conducted for the lower energy cut of the (110) oxide surface. Electrostatic potentials are calculated for AIMD snapshots sampled every 100 time steps during a 40.0 ps trajectory for the smaller, and during a 20.6 ps run for a larger cell with more water, and are averaged. They are not computed every time step partly

due to computational cost, and partly because the electrostatic profile should not change significantly every 0.5 fs. Atoms in the AIMD simulation cells are not constrained; the spatial drifts of the oxide slab during AIMD trajectories are negligible. Water dipole orientation times can be significant on metal surfaces.⁵⁴ Our hydrophilic oxide surfaces, however, with its more well-defined H-bond accepting and donating sites, likely form more well-defined hydrogen bond networks with less global fluctuations, than pristine metal surfaces.

Pure water|vacuum interfacial configurations for Fig. 1d are taken from Ref. 55. In that work, we used atomic positions generated with classical force field, took 110 snapshots, and averaged the electrostatic potential. Pseudopotential core region shifts were applied there to yield a zero potential outside noble atom cores,⁵⁷ although an “uncorrected” result of 2.80 V was also reported. In this work, we recompute the electrostatic profile without the corrections, using the standard VASP procedure for calculating work functions (“LVHAR=.TRUE.”) to ensure consistency and a proper cancellation of unwanted contributions from the interface with vacuum. We stress that the value of this water|vapor interfacial contribution is strictly a DFT construct.⁵⁵ It cannot be compared with the measured surface potential of water, because DFT calculations samples spatial regions inside the electron cloud of water molecules, unlike electrochemical measurements which involve the electrostatic potential experienced by ions that do not penetrate the interior of water molecules.^{55,58} Standard DFT work function calculations in vacuum (Fig. 4a contribution) also sample the interior of atomic nuclei because they measure electronic, not ionic, properties.

Isolated, charge-neutral V_O ’s are introduced by removing one oxygen atom each at various positions in a $3 \times 2 \times 2$ bulk crystalline oxide supercell. There are several types of oxygen sites in γ - Al_2O_3 , with some coordinated to three Al^{3+} ions and some to four. All 24 possible V_O defects in the primitive cell are considered. We stress that the γ - Al_2O_3 model, and its oxygen vacancies, are meant as model structures. The true passivating oxides are typically amorphous; until detailed experimental information about their structures is available, our approach is to use model systems to elucidate voltage-function relations. For the same reason, we do not focus on vacancy formation energies,⁵⁶ or in general ‘structure-function relations,’ since the structures have not been elucidated at the atomic length scale.

system	dimensions	stoichiometry	k -sampling	Figure
Al(111) γ (110)	$8.41 \times 24.23 \times 40.00$	$\text{Al}_{294}\text{O}_{216}$	$3 \times 1 \times 1$	Fig. 2b
γ - Al_2O_3 (110) water	$16.82 \times 16.15 \times 32.00$	$\text{Al}_{128}\text{O}_{192}(\text{H}_2\text{O})_{202}$	$1 \times 1 \times 1$	Fig. 2c
γ - Al_2O_3 (110) water	$16.82 \times 16.15 \times 38.00$	$\text{Al}_{128}\text{O}_{192}(\text{H}_2\text{O})_{250}$	$1 \times 1 \times 1$	Fig. 2c
γ - Al_2O_3 (110)* water	$16.82 \times 16.15 \times 35.00$	$\text{Al}_{128}\text{O}_{192}(\text{H}_2\text{O})_{203}$	$1 \times 1 \times 1$	Fig. 2c
water vacuum	$10.00 \times 10.00 \times 26.00$	$(\text{H}_2\text{O})_{32}$	$3 \times 1 \times 1$	Fig. 2d
γ - Al_2O_3 (110) vacuum	$8.41 \times 24.23 \times 40.00$	$\text{Al}_{144}\text{O}_{216}$	$3 \times 1 \times 1$	Fig. 2e
$\text{Al}(\text{OH})_3$ water	$17.86 \times 10.03 \times 38.00$	$(\text{Al}(\text{OH})_3)_{48}(\text{H}_2\text{O})_{145}$	$1 \times 1 \times 1$	Fig. 7b
γ - Al_2O_3	$16.75 \times 16.82 \times 16.15$	$\text{Al}_{192}\text{O}_{288}$	$1 \times 1 \times 1$	Fig. 8

TABLE I: Computational details of the main simulation cells. Dimensions are in units of \AA^3 . *A higher surface energy cut of the slab (“B-cut”).

B. Band Alignment and Voltage

DFT is an electronic structure ground state theory and supports only one E_F . The most readily available reference “electrode” is vacuum (Fig. 1a). Following the Trasatti convention,⁵⁹ we define the absolute voltage referenced against SHE (\mathcal{V}_e) to be

$$\mathcal{V}_e = W/|e| - 4.44 \text{ V}, \quad (1)$$

where $|e|$ is the electronic charge, $W = -E_F$ is the work function, and E_F is referenced to vacuum. In general, the work function is cumulatively modified by the electric double layer (EDL) and/or contact potential at each interface,³¹ as well as the electric field inside the electrolyte and electrode. Under our flat band conditions, the interfaces are uncharged and there is no electric field. Assuming the oxide and water regions are sufficiently thick, the electrostatic potential contributions (ϕ) should be additive:

$$\phi = (\phi_{\text{mf}} + \phi_{\text{fv}}) + \phi_{\text{fs}} - \phi_{\text{fv}} + \phi_{\text{sv}}, \quad (2)$$

where “m,” “f,” “s,” and “v” stands for metal, (oxide) film, solvent, and vacuum, respectively, and the four terms on the right correspond to panels (b)-(e) in Fig. 1. Adding $-\phi_{\text{fv}}$ cancels the oxide|vacuum contribution that is present in Fig. 1b which should not exist in the true model system (Fig. 1a). Fig. 1c (ϕ_{fs}) represents the only calculation without a vacuum

region; instead the plateau electrostatic reference value is extracted from the middle of the liquid region.

To our knowledge, only PZC’s on pristine metal surfaces have been computed⁸ using AIMD methods developed for redox potential and pK_a calculations.^{8,60,62} For example, Ref. 8 applies a “computational hydrogen electrode” (CHE) approach to calculate the PZC of metals without surface oxides, instead of relying on the Trasatti relation. For our system, this approach would require both metal|oxide and oxide|water interfaces in the same simulation cell, which is computationally costly. This is one reason we have used an alternate method. Note that, even on pristine metal surfaces, implicit solvent models have been more frequently applied to calculating PZC’s.^{7,10} With an eye to future studies based on these models, we do not align the metal|oxide interface using symmetric slab models without vacuum regions.⁶¹ The oxide|vacuum (or electrolyte) interface plays significant roles in corrosion and related disciplines,^{6,33} and will be the focus of future work based on our models.

The experimental approach used to determine the PZC is qualitatively different from the DFT approach. Bockris *et al.* modeled the passivating oxide as a semiconductor.¹¹ The Fermi level was assumed to be pinned at defect orbital levels, and the metal region was omitted. A Mott-Schottky approach was applied to vary the applied voltage to interpolate the potential towards the vanishing “depletion layer” thickness condition associated with the PZC. One possible limitation of this approach is that, far away from the PZC, the interpolation procedure assumed depletion layer widths that may exceed the passivating oxide thickness.³⁷ DFT calculations typically apply simulation cells with crystalline oxide films with no or few defects, unlike experimental oxide samples which exhibit a range of defect level energies. As a result, a metal “electrode” is generally needed to determine the DFT Fermi level.^{6,15,16}

III. RESULTS

A. Oxide|Vacuum Interface

Fig. 2a-b depicts the A- and B-cuts of γ -Al₂O₃ (110) symmetric slabs, with the atomic coordinates relaxed to their lowest energy configurations. The A-cut structure is consistent with Ref. 48 and gives a surface energy of 1.53 J/nm², within 0.01 J/nm² of the previous

literature value.⁴⁸ The B-cut has a slightly higher surface energy of 1.76 J/nm².

B. Al|Oxide Interface (Fig 1b)

Fig. 2c-d depict an A-cut directly optimized on the Al(111) surface, and an A-cut oxide slab annealed with AIMD prior to optimization, respectively. The entire length of the oxide-only simulation cell is depicted in Fig. 2e. The AIMD-annealed metal|oxide interface configuration is more favorable by 1.50 eV, due to the formation of two more Al-O ionic bonds at the interface per simulation cell. The work functions are 4.05 eV and 4.18 eV before and after annealing, respectively. This shows that the AIMD-induced change in interfacial dipole surface density is small, partly due to the fact that the increase in bonding is averaged over the significant surface area of the simulation cell.

The bare Al(111) surface at this lattice constant has a work function of 3.97 eV when computed using the PBE functional. Hence the contact potential, which is the difference between work functions of the metal in contact/not in contact with an oxide film without a permanent dipole moment³² divided by $|e|$, is a modest +0.21 V for the AIMD-annealed (110) cut. This is small compared to other metal oxide interfaces examined in the DFT literature.^{14,32} Our previous work on the α -Al₂O₃(001)|vacuum interface predicts a -1 eV contact potential;⁶ the larger value there likely arises from the more extensive metal-oxide contacts at that interface, which has a higher surface atom density.

As discussed in the Method section, we have also performed a limited grid search on the registry between metal and oxide, without AIMD equilibration. The total energies of these simulation cells are less favorable than the AIMD-relaxed slab by 1.74±0.06 eV. The most and least favorable of these optimized configurations are 1.00 and 3.21 eV less favorable than the AIMD-relaxed configuration. The work functions range from 3.92 to 4.23 eV, averaging to within 0.06±0.01 eV of the AIMD-relaxed slab value (4.18 eV).

Assuming that the overall variation of work functional with B-cut interfacial structure is also small, we only conduct one work function calculation on one B-cut structure without annealing. We obtain a 4.02 eV work function, which is only 0.16 eV lower than that for the the AIMD-relaxed A-cut configuration. This suggests that the work function, and voltage according to Eq. 1, is not as strongly dependent on the details of the metal| γ -Al₂O₃ and/or the γ -Al₂O₃|vacuum interfaces, as in the case of α -Al₂O₃.⁶

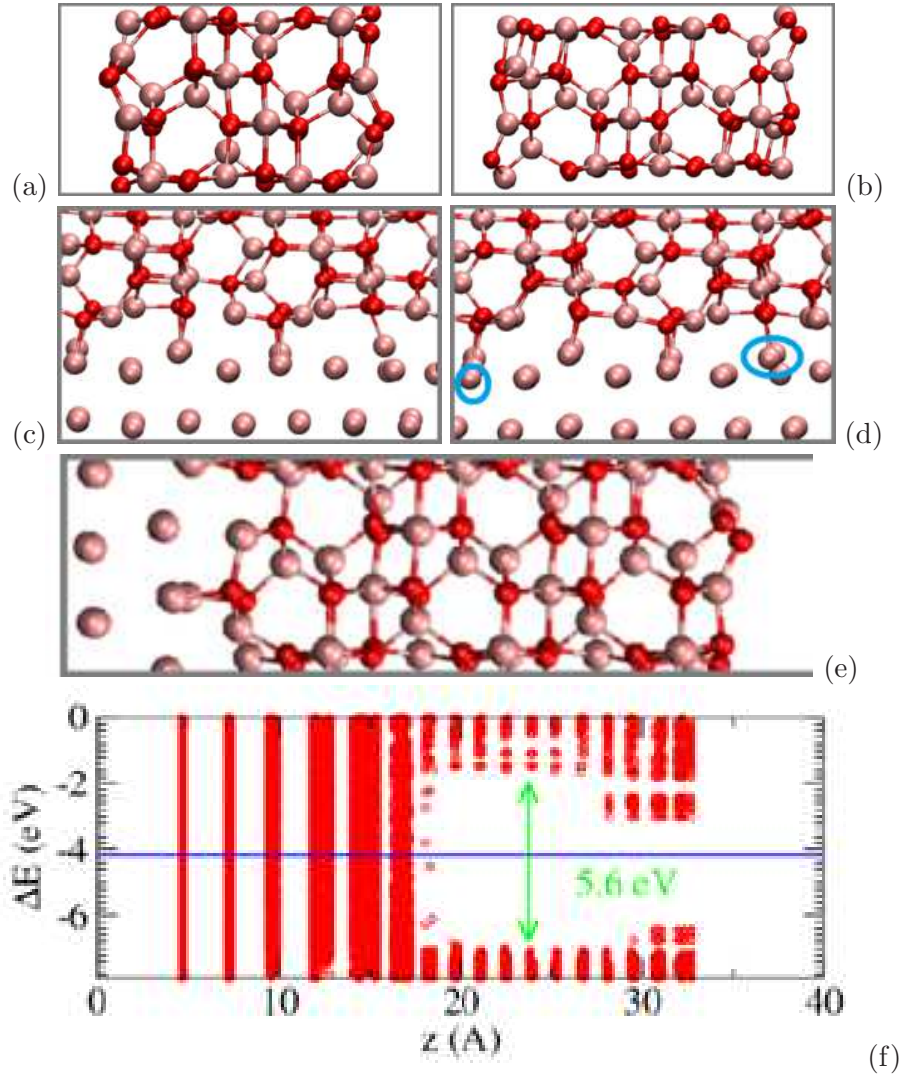


FIG. 2: (a) A-cut γ -Al₂O₃ (110); (b) B-cut γ -Al₂O₃ (110). (c)-(d) A-cut on Al(111) with/without AIMD pre-equilibration. The vacuum region atop the oxide layer is not shown. There are two extra Al-O ionic bond in (c) than in (d), shown in blue circles. (e) The entire length of the AIMD-annealed A-cut slab. (f) Local density of state associated with panel (d). The Al region ($z < 18$ Å) exhibits no band gap while the interior of the oxide region ($z > 18$ Å) exhibits a ~ 5.6 eV gap, which is very similar to that computed for bulk γ -Al₂O₃ using the PBE functional. Pink, red, and white spheres represent Al, O, and H atoms, respectively.

C. Oxide|Water Interface (Fig. 1c-d)

Fig. 3a-c depict snapshots of AIMD simulations of the A- and B-cuts of γ -Al₂O₃ immersed in water. The corresponding electrostatic potential profiles ($\phi(z)$), averaged in the x - and

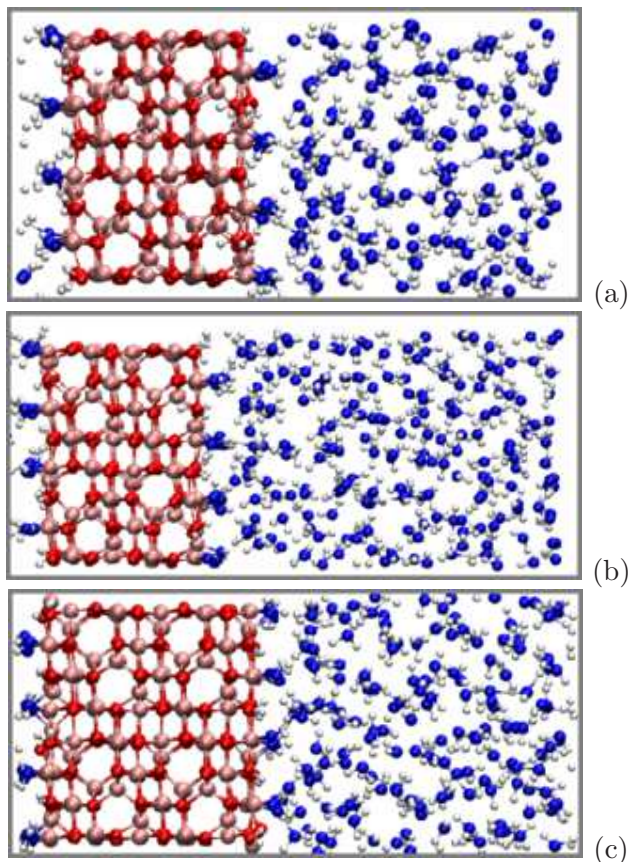


FIG. 3: Snapshot of the interface between water and (a) A-cut γ - Al_2O_3 (110); (b) same as (a) but with a thicker layer of water; (c) B-cut γ - Al_2O_3 (110). Pink, red, blue, and white spheres represent Al, O, O(water), and H atoms, respectively

y -directions, are depicted in Fig. 4a-c, where results in vacuum and in water are compared. Only relative values in $\phi(z)$ are significant; indeed the vacuum curves are shifted in voltage scale to match the solid state region of the slab with water.

We integrate $-|e|\phi(z)$ in the oxide interior demarcated by the arrows in Fig. 4, and $-|e|\phi(z)$ in the water or vacuum plateau region demarcated by the arrows there. Then we subtract the vacuum result from the water value. The shift in $-|e|\phi_{\text{fs}}$ is -4.47 V for the smaller A-cut model (Fig. 3a, 4a). In the B-cut (Fig. 3c, 4c), they are -4.92 V. $\phi(z)$ in the aqueous region is not perfectly flat even when z farthest from the solid surfaces. This reflects a slightly incomplete sampling of the aqueous configurations of the γ - Al_2O_3 |water interfaces as well as the finite size of the water region. To examine finite size effects, we also consider an A-cut simulation cell with a water film that is 6 Å thick (Fig. 3b). The shift between vacuum and water termination is -4.31 V (Fig. 4b), which is within 0.16 V of the

system with a thinner water slab on this surface (Fig. 4a). Henceforth we will report the 4.31 V associated with the larger simulation cell; and treat the difference of 0.16 V between the two cell sizes as a possible system size effect/systematic uncertainty in our calculations. $-|e|\Delta\phi_{fs}=-4.31$ eV and -4.92 eV are added to the work functions reported in the last section to obtain shifts arising from the oxide/water (“*fs*”) interfaces. These “work functions” of the A- and B-cut oxide-covered Al metal slabs become -0.13 eV and -0.70 eV, respectively. However, the test electron associated with these values are ejected into the aqueous region (not vacuum). Therefore these values cannot be compared with experiments.

During AIMD simulations, we observe two OH groups point inwards, towards the oxide interior, in the A-cut. This is not observed in the monolayer water configuration on this surface.⁴⁸ However, these OH groups exhibit no tendency of transferring their protons from the O-anions on the oxide surface, which are coordinated to two Al^{3+} , to interior O-anions coordinated to at least three Al^{3+} .

D. Water|Vacuum Interface (Fig. 1e)

For this interface, we compute $\phi(z)$ by averaging the electrostatic profiles of a set of 110 classical force field water configurations from previous calculations.⁵⁵ Fig. 5 depicts the average $\phi(z)$. The small, 0.01 V/Å slope observed in the vacuum region is due to incomplete sampling, resulting in a small net dipole moment in the water slab. We take the value at the center of the vacuum region as the plateau value to calculate the $\phi(x)$ shift between water and vacuum, yielding $\Delta\phi=+2.80$ V going from liquid water to vacuum. The water density in this model slab is actually 0.92 g/cm³,⁵⁵ not the canonical 1.0 g/cm⁻³ value, and the the potential difference should be proportional to the water density, we further scale $\Delta\phi$ by $1/0.92$, arriving at $\Delta\phi=3.04$ V. Note the classical force field MD trajectory used to generate the configurations for DFT snapshot calculations use a simulation cell with 12.5 Å lateral dimensions (perpendicular to the interface). The dispersion force cutoff for the force field MD is less than half the lateral box size, which results in the lower density.

The significance of this $+3.04$ V shift is as follows. There is no vacuum region or water/vacuum interface in Fig. 1c. If there were, the electrostatic potential would be shifted by $+3.04$ V. With this prediction, and using results from the last section, Fig. 1c, d, and e combine to give work functions of $+2.91$ eV and 2.34 eV, respectively, for the water-covered

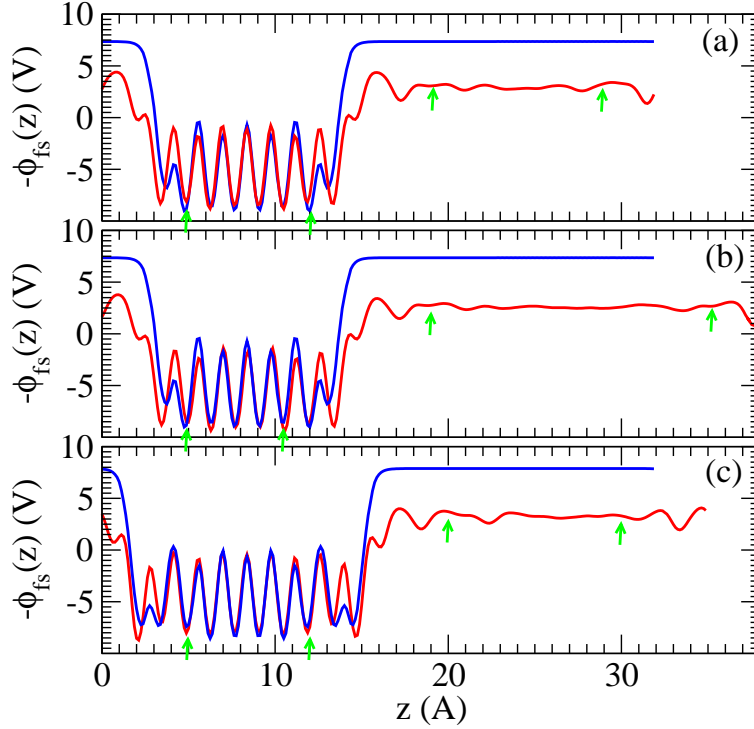


FIG. 4: Electrostatic potential profiles ($\phi(z)$) between γ -Al₂O₃ (110) and water (red) or vacuum (blue). (a) and (c) are for the A- and B-cuts, respectively. (b) is similar to (a) but has a thicker water region.

A- and B-cuts. In principal, these are measurable work functions, because the test electrons are now ejected into the vacuum.

E. Combining All Contributions

Converting the water-modified work functions to voltages using Eq. 1, we obtain -1.53 V and -2.10 V vs. SHE for the A- (Fig. 6) and B-cuts, respectively. The former value, computed using the most stable γ -Al₂O₃ (110) surface, is 0.52 V more negative than -1.01 V reported in Ref. 11. The other reported experimental value (-0.7 vs. SHE) is even smaller in magnitude.³ The B-cut value, computed using a higher (110) surface, is substantially more negative still.

We predicted a -1.98 V vs. SHE PZC value for α -Al₂O₃(001)|vacuum interface when a frozen monolayer of partially hydrolyzed H₂O exists on that interface.⁶ However, as discussed

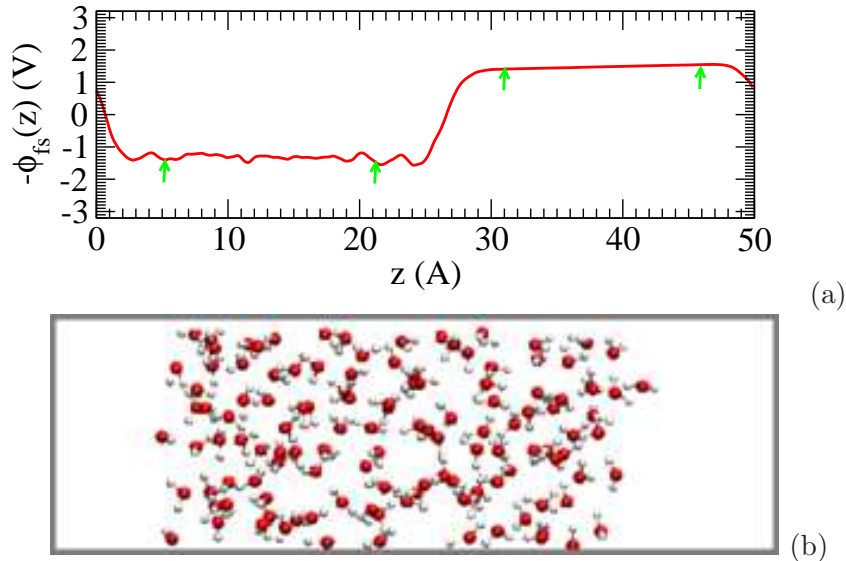


FIG. 5: (a) Electrostatic potential profiles ($\phi(z)$) at the water-vacuum interface. (b) Snapshot of the water/vacuum interface. Red and white spheres represent O and H atoms, respectively.

earlier, the voltage predicted there is too sensitive to the configuration of the frozen H_2O molecules to be reliable. In this work, the H_2O configurations are sampled via AIMD simulations and should be correctly governed by the Boltzmann distribution. If we omit the liquid water contribution and only use the single frozen layer of water of Ref. 48, the electrostatic potential shift would only consist of the Fig. 1b contribution, plus the difference between Fig. 1d with and without the frozen surface water layer. The work function shift due to adding the frozen water layer is computed using a potential plot like Fig. 4a (not shown). It is -1.13 eV. This correction reduces the work function of Fig. 1b to 3.05 eV. Using Eq. 1, this translates into a PZC of -1.39 V, which differ from the AIMD predictions by only +0.14 V. This shows that, for this $\gamma\text{-Al}_2\text{O}_3$ (110) surface, the predicted voltage does not appear overly sensitive to the surface water content, unlike $\alpha\text{-Al}_2\text{O}_3$ (111).

We propose that the discrepancy between the experimental and the DFT PZC is not mainly due to uncertainties in the DFT calculations, or the fact that the experimental work used the Mott-Schottky plot which requires extrapolation from oxide film thicknesses that are beyond typical alumina film thicknesses on Al metal.¹¹ Instead, we argue that discrepancy arises from differences in the oxide stoichiometry. The oxide films of Ref. 11

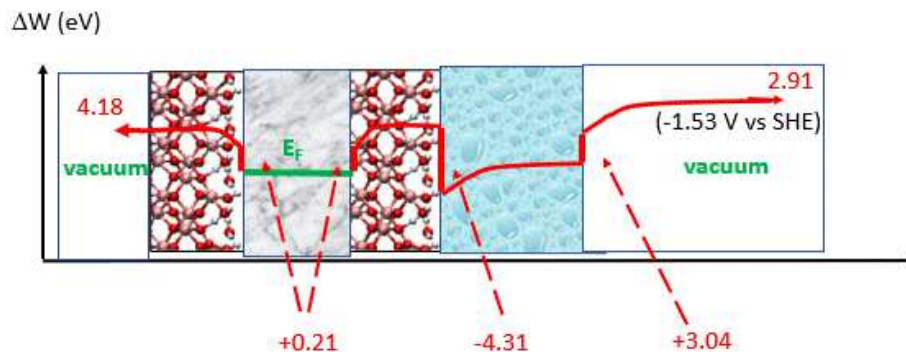


FIG. 6: Schematic summary of the work function shifts at different interfaces, not drawn to scale.

has Al:O atomic ratios which vary with oxide depth. The ratio should be 1:1.5 for ideal Al_2O_3 , and close to the metal|oxide interface this ratio is indeed observed. However, near the oxide|water interface, this ratio can reach 1.8 to 2.0.¹¹ This is rationalized by the presence of protons, i.e., oxy-hydroxide content. Three H^+ need to substitute for each Al^{3+} to attain charge neutrality. Another possibility is that net charges exist inside the oxide film.¹¹ Our crystalline $\gamma\text{-Al}_2\text{O}_3$ oxide film model is not equipped to deal with this latter possibility; we will defer investigation of space charge effects and amorphous oxide models to future work.

Two common forms of crystalline oxy-hydroxides are gibbsite ($\text{Al}(\text{OH})_3$) and boehmite (AlOOH).⁶³ Next we re-examine the difference between the oxide|water (Fig. 1c) and oxide|vacuum (Fig. 1d) contributions by substituting a $\text{Al}(\text{OH})_3$ (001) slab⁶³ for the $\gamma\text{-Al}_2\text{O}_3$ slab. This gibbsite model has the maximal hydrogen content possible, and serves as a limiting case. Fig. 7a compares the electrostatic potentials computed for $\text{Al}(\text{OH})_3$ (001) in the presence (snapshot shown in Fig. 7b) and absence of water, respectively. The difference in the plateau region is -3.18 V. This is significantly less negative than the -4.31 V for the $\gamma\text{-Al}_2\text{O}_3$ (110) A-cut surface. If we simply apply -3.18 V to the previous compilation of interfacial contributions, we obtain a PZC value of -0.40 V instead of -1.53 V. This value is now substantially too positive, rather than too negative, compared with experiments. It shifts the predicted PZC in the right direction, but overcorrects it.

This is a qualitative demonstration. We have not attempted to calculate the Fig. 1b contribution with $\text{Al}(\text{OH})_3$ (001) because $\text{Al}(\text{OH})_3$ is thermodynamically unstable with respect to Al metal and should react to form H_2 gas. Furthermore, the hydrogen content deduced in experiments is not as high as in $\text{Al}(\text{OH})_3$, which has a Al:O ratio of 1:3. Hence the difference

between γ -Al₂O₃ and Al(OH)₃ is overestimated relative to experiments. Nevertheless, Fig. 7 is evocative and suggests that hydrogen content in the film – not just as hydroxyl groups on the surface layer but in subsurface oxide layers as well – can have significant effects on the PZC.

Given the lack of definitive experimental oxide film structure and stoichiometry at the atomic length scale, we propose the following perspective. Each DFT-based model with a specific passivating oxide structure and interfaces should be considered a model system with an intrinsic PZC. The corrosion onset potential and other corrosion-related properties should be referenced to this PZC rather than the experimental value. For better comparison with experiments, we should devise atomic length-scale models that yield the experimental PZC.

F. Oxygen Vacancy Orbital Level

Finally, we elucidate the conditions under which oxygen vacancies may have net positive charges in our model (Fig. 1f). Such charged vacancies are foundational within the PDM corrosion theory.⁵ As in Ref. 6, we define $E_{V_O VBE}$ to be the V_O energy level above the oxide valence band edge (VBE), and E_{FVBE} as the difference between the VBE energy level and the Fermi level (E_F). The former is computed in simulation cells without Al metal, while the latter is only relevant for simulation cells with metal electrodes. From Fig. 2f, the local density of state (LDOS) for the configuration of Fig. 2d, we find that $E_{FVBE}=2.89$ eV in the “bulk-like” region of the oxide in Fig. 2f ($20 \text{ \AA} < z < 29 \text{ \AA}$), but is 2.26 eV near the oxide outer surface ($z > 29 \text{ \AA}$). The LDOS is constructed by decomposition both occupied and unoccupied orbitals on to atomic contributions.⁶⁴

Fig. 8c depicts $E_{V_O VBE}$ for the 24 possible distinct V_O in the bulk γ -Al₂O₃ supercell (Table I). Unlike α -Al₂O₃, not all O-sites are equivalent; some O atoms in the crystal are 3-coordinated while others are 4-coordinated. The defect orbital levels reside in 4 bands centering around 1.1, 1.3, 1.4, and 1.6 eV above the VBE. The highest-lying defect orbitals correspond to 4-coordinated O-sites. The V_O formation energies of these defects (not orbital levels) span a range of 0.28 eV. For our calculations, we pick the highest lying defect orbital level so that, if this V_O is occupied by electrons and charge-neutral, all other V_O choices are also charge-neutral. This yields $E_{V_O VBE}=1.60$ eV.

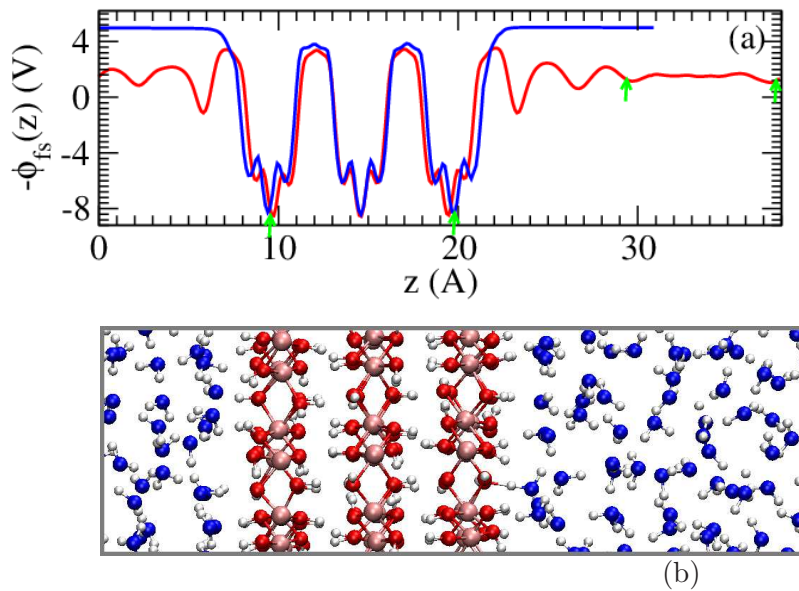


FIG. 7: (a) Electrostatic potential profiles ($\phi(z)$) at the water- $\text{Al}(\text{OH})_3$ (001) interface. Red and blue are with/without water, respectively. (b) Snapshot of the gibbsite (001)/water interfacial configuration. Pink, red, blue, and white spheres represent Al, O, O(water), and H atoms, respectively

To translate the E_{V_0VBE} predictions to the E_{FVBE} associated with the metal/oxide/water PZC configuration (Fig. 1a via Fig. 1b-d), we subtract the 1.60 eV relevant to the highest charge-neutral vacancy orbital energy level from E_{FVBE} , yielding 1.29 eV in the oxide interior and 0.66 eV near the oxide outer surface. This means that all V_O are at least 1.29 eV/0.66 eV below the Fermi level at PZC conditions (Fig. 8a-b); they all contain defect orbitals occupied by electrons and are charge-neutral. This assessment qualitatively agrees with $\alpha\text{-Al}_2\text{O}_3$,

where the V_O level is 0.60 eV below the Fermi level.⁶

The PZC is estimated above to be -1.53 V vs. SHE. To push O-vacancy orbitals in the oxide interior above the Fermi level, so that they acquire positive charges, requires raising the voltage by at least 1.29 V, to -0.24 V vs. SHE. The -0.24 V value for this model similar to the measured onset potential of pitting in Al metals of \sim -0.3 V,¹¹ although it is higher than the minimum pitting potential of -0.50 V reported elsewhere.¹³ At or above -0.24 V, our model system would exhibit V_O^{2+} . If we had used the experimental PZC of \sim -1.0 V, a value of +0.29 V would be needed to create V_O^{2+} , which is significantly above the experimental pitting potential of -0.3 V. As discussed above, for internal consistency, we should use the computed PZC to characterize oxide film properties like V_O orbital levels in DFT models. For O vacancies oxide near the oxide outer surface in Fig. 2f, V_O^{2+} can occur at much lower potentials of $(-1.53+0.66)=-0.87$ V.

This above estimates are derived using the flat-band approximation, where the oxide film electrostatic potential is raised uniformly with increasing applied potential. In reality, when a charged surface (e.g., enhanced ion concentrations in EDL in the liquid electrolyte) exists to raise the overall voltage, the oxide region near the liquid electrolyte is at higher energy levels than the region near the metal surface due to the electric field across the oxide film. Hence the outer region of the passivating oxide may begin to exhibit oxygen vacancies that are positively charged at lower potentials than those near the metal surface.

Finally, we address DFT functional accuracies. The more accurate HSE06 functional⁴³⁻⁴⁵ was previously applied to spot-check PBE predictions for the Al(111)| α -Al₂O₃ (111) model.⁶ Compared to PBE calculations, the V_O orbital level was found to shift up into the band gap by $\Delta E_{V_O VBE}=0.78$ eV. For the bulk γ -Al₂O₃ 3 \times 2 \times 2 supercell, we find that HSE06 predicts $E_{V_O VBE}=2.25$ eV at one of the V_O site where PBE predicts $E_{V_O VBE}=1.60$ eV. Thus $\Delta E_{V_O VBE}$ is 0.65 eV, which is reasonably similar to the 0.78 eV value predicted for α -Al₂O₃.

HSE06 also shifted the VBE edge downwards relative to E_F , i.e., it increased ΔE_{FVBE} for Al(111)| α -Al₂O₃ (111), by 1.14 eV. The net effect was a downward revision of the occupied V_O vacancy level by 0.36 eV. Unfortunately, the Al(111)| γ -Al₂O₃ (110) interface model simulation cell (Table I), which is a focus of the present work, is too large to permit a HSE06 spot check of E_{FVBE} .

If we assume the overall magnitude of the HSE06 correction to PBE for α -Al₂O₃ also corrects for the current γ -Al₂O₃ system, it would further lower the V_O orbital energy by

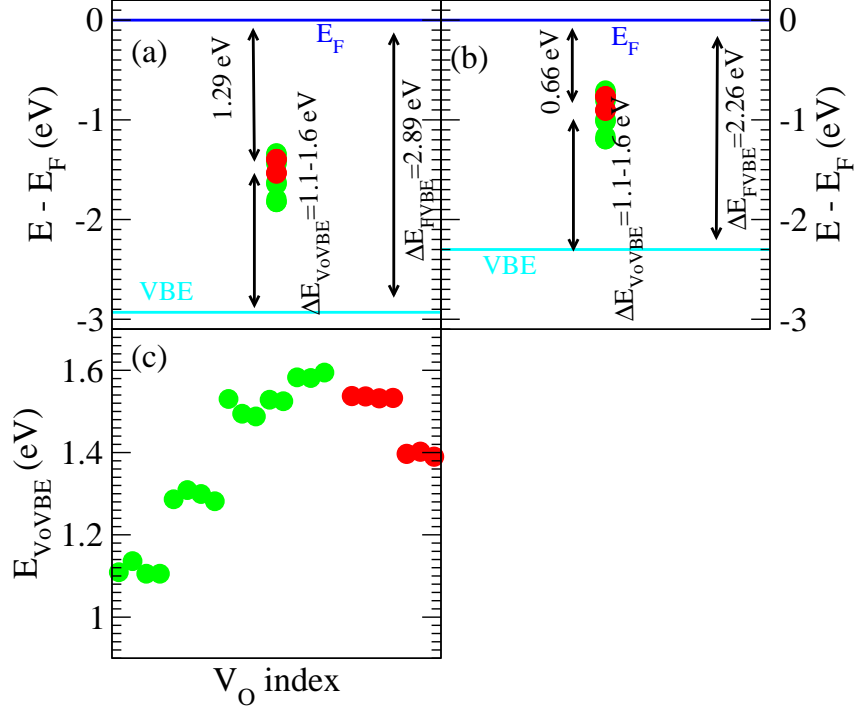


FIG. 8: (a)-(b) Schematic aligning the charge-neutral V_O orbital levels to the metal E_F , for the bulk-like and surface oxide regions of Fig. 2f), respectively. (c) Orbital levels for the 24 distinct optimized vacancies, relative to the VBE. Red and green refer to 3- and 4-coordinated O-sites, respectively.

0.36 V relative to E_F , compared to PBE values. With this correction, it would require an extra +0.36 V, or a total of -0.51 V instead of -0.87 V, to raise the V_O level above E_F in the outer oxide region. While this value is still within the range of the -0.5 V pitting onset potential for aluminum,¹³ the interior of the oxide would require at least $(-0.24+0.36)=+0.12$ V to acquire positive charges. This semi-quantitative discussion of DFT accuracy appears to reinforce our conclusion that the outer regions of the oxide is more likely to support V_O^{2+} vacancies. However, as the oxide starts to break down from its outer, electrolyte-facing surface, the interior regions should become more “surface-like” and become more susceptible to creation of V_O^{2+} .

IV. CONCLUSION

In this work, we have applied DFT/PBE methods to calculate the potential-of-zero-charge (PZC) of a model system relevant to aluminum corrosion. Our models consist of Al(111) slabs covered with thin, low energy cuts of γ -Al₂O₃ (110) films immersed in liquid water. They mimic Al metal passivated with amorphous oxide films in contact with multiple layers of water, which are relevant to both inundated and high-humidity atmospheric corrosion conditions. The models have no explicit surface charge either on the metal or the oxide film surface and are therefore simultaneously at the PZC of the electrode and the pH-of-zero-charge of the oxide. By splitting this system with two interfaces into multiple binary systems with one interface each, and summing the contributions, we predict that the PZC resides at -1.53 V vs. SHE. The systematic error may be on the order of 0.16 V and is mostly attributed to AIMD simulations of liquid water at Al₂O₃ surfaces. The prediction is more negative than the \sim -0.7 to -1.0 V experimental values reported in the literature.^{3,11} Using a higher energy cut of the (110) surface slightly alters the DFT predicted PZC value to an even more negative -2.10 V, which is a measure of the variation of PZC with interfacial structure. We argue that the predicted PZC value is too negative because the DFT oxide model lacks sufficient proton content.¹¹ Adopting the other extreme, namely a gibbsite surface film (Al(OH)₃) with too much hydrogen content compared to measurements, indeed yields a significantly more positive PZC of -0.49 V.

Under our PZC condition, the highest lying oxygen vacancy (V_O) orbital level resides at 1.29 to 0.66 eV below the Fermi level, depending on whether the vacancy is in the oxide interior or near the oxide|electrolyte interface. Within a flat-band approximation, this implies that raising the potential above -0.24 V or -0.87 V vs. SHE is sufficient to raise the V_O orbitals above the Fermi level and render at least some oxygen vacancies positively charged. V_O^{2+} are integral parts of the point defect model, one of the theories widely used to analyze pitting corrosion kinetics.⁵ Our predictions for oxygen vacancy near the oxide outer surface are consistent with the PDM assumption that the reported minimal onset potential for pitting for Al of -0.5 V vs. SHE,¹³ which is higher than the -0.87 V needed to create V_O^{2+} there. We argue that, as the passivation oxide starts to break down, more of the interior oxide becomes surface-like and becomes more susceptible to V_O^{2+} formation. Future work along these lines will involve inclusion of an explicit electric field across the oxide,

which enhances V_{O}^{2+} creation in the oxide film near the liquid electrolyte but less so near the metal surface; and the consideration of true amorphous oxide models, which may yield a wider distribution of V_{O} orbital levels than the $\gamma\text{-Al}_2\text{O}_3$ model applied in this work, as well as a non-zero space charge inside the oxide. Computationally speaking, we find that each aluminum metal/passivating oxide DFT model exhibits a different PZC. In the future, we should construct interfacial models with predicted PZC's that agree with the experimental value. In other words, the computed PZC should be used as a constraint on the model, not treated as a prediction. Finally, this work also provides a benchmark for future implicit solvent calculations.¹²

Acknowledgement

We thank Anastasia Ilgen, Jacob Harvey, and Quinn Campbell for useful suggestions. This work is funded by the Advanced Strategic Computing (ASC) Program. Sandia National Laboratories is a multi-mission laboratory managed and operated by National Technology and Engineering Solutions of Sandia, LLC, a wholly owned subsidiary of Honeywell International, Inc., for the U.S. Department of Energy's National Nuclear Security Administration under contract DE-NA0003525. This paper describes objective technical results and analysis. Any subjective views or opinions that might be expressed in the document do not necessarily represent the views of the U.S. Department of Energy or the United States Government.

¹ R.W. Revie (eds) *Uhlig's Corrosion Handbook*, Third Edition. (Wiley, 2011)

² E. McCafferty, *Electrochim. Acta* **55**, 1630-1637 (2010).

³ E. McCafferty, *J. Electrochem. Soc.* **146**, 2863 (1999).

⁴ P.M. Natishan, E. McCafferty, and G.K. Hubler, *J. Electrochem. Soc.* **135**, 321 (1988)

⁵ C.Y. Chao, L.F. Lin, and D.D. Macdonald, *J. Electrochem. Soc.* **128**, 1187 (1981).

⁶ K. Leung, *J. Electrochem. Soc.* **168**, 031511 (2021).

⁷ K. Letchworth-Weaver and T.A. Arias, *Phys. Rev. B*, **86**, 075140 (2012).

⁸ X.-Y. Li, A. Chen, X.-H. Yang, J.-X. Zhu, J.-B. Le, and J. Cheng, *J. Phys. Chem. Lett.* **12**,

- 7299 (2021).
- ⁹ C.D. Taylor, M.J. Janik, M. Neurock, and R.G. Kelly, *Mol. Sim.* **33**, 429 (2007).
 - ¹⁰ K. Kano, S. Hagiwara, T. Igarashi, and M. Otani, *Electrochim. Acta* **377**, 138121 (2021).
 - ¹¹ J.O'M. Bockris, and Y.K. Kang, *J. Solid State Electrochem.* **1**, 17 (1997).
 - ¹² Q. Campbell and I. Dabo, *Phys. Rev. B*, **96**, 205308 (2017).
 - ¹³ J.B. Bessone, D.R. Salinas, C.E. Mayer, M. Ebert & W.J. Lorenz, *Electrochim. Acta* **37**, 2283 (1992).
 - ¹⁴ X.-X. Yu, and L.D. Marks, *Corrosion*, **75**, 152-166 (2019).
 - ¹⁵ P. Cornette, D. Costa, and P. Marcus, *J. Electrochem. Soc.* **167**, 161501 (2020).
 - ¹⁶ D. Costa, T. Ribeiro, P. Cornette, and P. Marcus, *J. Phys. Chem. C*, **120**, 28607 (2016).
 - ¹⁷ D. Costa, T. Ribeiro, F. Mercuri, G. Pacchioni, and P. Marcus, *Adv. Mater. Interfaces* **1**, 1300072 (2014).
 - ¹⁸ M. Li, Y. Jin, B. Chen, C. Leygraf, L. Wang, and J. Pan, *J. Electrochem. Soc.* **168**, 081508 (2021).
 - ¹⁹ M. Kadowaki, A. Saengdeejing, I. Muto, Y. Chen, T. Doi, K. Kawano, Y. Sugawara, and N. Hara, *J. Electrochem. Soc.* **168**, 111503 (2021).
 - ²⁰ L.F. Lin, C.Y. Chao, and D.D. Macdonald, *J. Electrochem. Soc.* **128**, 1194 (1981).
 - ²¹ D.D. Macdonald and X. Lei. *J. Electrochem. Soc.*, **163** C738 (2016).
 - ²² S. Sharifi-Asl, F. Mao, P. Lu, B. Kursten, and D.D. Macdonald. *Corrosion Sci.* **98**, 708 (2015).
 - ²³ P. Lu, R. Engelhardt, B. Kursten, and D.D. Macdonald. *J. Electrochem. Soc.* **163** C156 (2016).
 - ²⁴ G.S. Frankel, *J. Electrochem. Soc.* **145**, 2186 (1998).
 - ²⁵ M. Bojinov, G. Fabricius, T. Laitinen, K. Makela, T. Saario, and G. Sundholm, *Electrochim. Acta* **45**, 2029 (2000).
 - ²⁶ A. Seyeux, V. Maurice, and P. Marcus, *J. Electrom. Soc.* **160**, C189 (2013).
 - ²⁷ A. Couet, A.T. Motta, and A. Ambard, *Corros. Sci.* **100**, 73 (2015).
 - ²⁸ A. Momeni and J.C. Wren, *Faraday Discuss.* **180**, 113 (2015).
 - ²⁹ C. Batallion, F. Bouchon, C. Chainais-Hillairet, C. Desgranges, E. Hoarau, F. Martin, S. Perrin, M. Tupin, and J. Talandier, *Electrochim. Acta* **55**, 4451 (2010).
 - ³⁰ E. McCafferty, *Corros. Sci.* **45**, 1421 (2003).
 - ³¹ N. Bonnet, T. Morishita, O. Sugino, and M. Otani, *Phys. Rev. Lett.*, **109**, 266101 (2012).
 - ³² K. Leung, *Phys. Chem. Chem. Phys.* **22**, 10412 (2020).

- ³³ K. Leung, L.C. Merrill, and K.L. Harrison, *J. Phys. Chem. C* **126**, 8565 (2022).
- ³⁴ O.A. Dicks, J. Cottom, A.L. Shluger, and V.V. Afanas'ev. *Nanotechnology* **30**, 205201 (2019).
- ³⁵ J. Strand, M. Kaviani, D. Gao, A. El-Sayed, V.V. Afanas'ev, and A.L. Shluger. *J. Phys.: Condens. Matter*, **30**, 233001 (2018).
- ³⁶ M. Aykol and K.A. Persson, *ACS Appl. Mater. Interfaces* **10**, 3039 (2018).
- ³⁷ J. Evertsson, F. Bertram, F. Zhang, L. Rullik, L.R. Merte, M. Shipilin, M. Soldemo, S. Ahmadi, N. Vinogradov, F. Carla, J. Weissenrieder, M. Göthelid, J. Pan, A. Mikkelsen, J.-O. Nilsson, and E. Lundgren, *Appl. Sur. Sci.* **349**, 826 (2015).
- ³⁸ G. Kresse and J. Furthmüller, *Phys. Rev. B*, **54**, 11169 (1996).
- ³⁹ G. Kresse and J. Furthmüller, *Comput. Mater. Sci.*, **6**, 15-50 (1996).
- ⁴⁰ G. Kresse and D. Joubert, *Phys. Rev. B*, **59**, 1758 (1999).
- ⁴¹ J. Paier, M. Marsman, and G. Kresse, *J. Chem. Phys.*, **127**, 024103 (2007).
- ⁴² J.P. Perdew, K. Burke, and M. Ernzerhof, *Phys. Rev. Lett.*, **77**, 3865 (1996).
- ⁴³ J. Heyd, G.E. Scuseria, and M. Ernzerhof, *J. Chem. Phys.*, **118**, 8207 (2003).
- ⁴⁴ J. Heyd, G.E. Scuseria, and M. Ernzerhof, *J. Chem. Phys.*, **124**, 219906 (2006).
- ⁴⁵ O.A. Vydrov, J. Heyd, A.V. Krukau, and G.E. Scuseria, *J. Chem. Phys.*, **125**, 074106 (2006).
- ⁴⁶ M. Marsman, J. Paier, A. Stroppa, and G. Kresse, *J. Phys. Condens. Matter*, **20**, 064201 (2008).
- ⁴⁷ See, e.g., E. Schwegler, J.C. Grossman, F. Gygi, and G. Galli, *J. Chem. Phys.*, **121**, 5400 (2004).
- ⁴⁸ B.F. Ngouana-Wakou, P. Cornette, M.C. Valero, D. Costa, and P. Raybaud, *J. Phys. Chem. C* **121**, 10351 (2017).
- ⁴⁹ M.G. Martin and A.P. Thompson, *A.P. Fluid Phase Equil.* **217**, 105 (2004).
- ⁵⁰ R.T. Cygan, J.-J. Liang, and A.G., Kalinichev *J. Phys. Chem. B* **108**, 1255, (2004).
- ⁵¹ Y.Y. Cheng, S.X. Lu, W.G. Xu, and H.D. Wen, *RSC Adv.* **5**, 15387 (2015).
- ⁵² R.M. Katona, S. Tokuda, J. Perry, and R.G. Kelly, *Corrosion Sci.* **175**, 108849 (2020).
- ⁵³ R.M. Katona, A.W. Knight, E.J. Schindelholz, C.R. Bryan, R.F. Schaller, and R.G. Kelly, *Electrochim. Acta* **370**, 137696 (2021).
- ⁵⁴ S. Sakong and A. Gross, *Phys. Chem. Chem. Phys.* **22**, 10431 (2020).
- ⁵⁵ K. Leung, *J. Phys. Chem. Lett.* **1**, 496 (2010).
- ⁵⁶ C. Freysoldt, B. Grabowski, T. Hickel, J. Neugebauer, G. Kresse, A. Janotti, and C.G. Van de Walle, *Rev. Mod. Phys.* **86**, 253 (2014).
- ⁵⁷ V.R. Saunders, C. Freyria-Fava, R. Dovesi, L. Salasco, C. Roetti, *Mol. Phys.* **77**, 629 (1992).

- ⁵⁸ S.M. Kathmann, I.F.W. Kuo, C.J. Mundy, and G.K. Schenter, *J. Phys. Chem. B* **115**, 4369 (2011).
- ⁵⁹ S. Trasatti, *J. Electroanal. Chem.* **209**, 417 (1986).
- ⁶⁰ J. Cheng, X. Liu, J. VandeVondele, M. Sulpizi, and M. Sprik. *Acc. Chem. Res.*, **47**, 3522 (2014).
- ⁶¹ S.-H. Yoo, N. Siemer, M. Todorova, D. Marx, and J. Neugebauer, *J. Phys. Chem. C* **123**, 5495 (2019).
- ⁶² J. Cheng and M. Sprik, *Phys. Chem. Chem. Phys.* **14**, 11245 (2012).
- ⁶³ M. Sassi, Z. Wang, E.D. Walter, X. Zhang, H. Zhang, X.S. Li, A. Tuladhar, M. Bowden, H.-F. Wang, S.B. Clark, and K.M. Rosso, *J. Phys. Chem. C* **124**, 5275 (2020).
- ⁶⁴ K. Leung and A. Leenheer, *J. Phys. Chem. C* **119**, 10234 (2015).